A Portable Femtoampere-Sensitive Readout System for a High-Pressure Argon Ionization Chamber

R. Bıyık, T. Yalçın, and O. Alaçayır

***Abstract*—This article presents the design, implementation, and validation of a portable femtoampere-sensitive electronic readout system for a high-pressure argon-filled ionization chamber (IC) radiation detector. The system integrates an ionization tube designed and fabricated at TENMAK laboratories as a part of this study together with a low-noise analog front-end, precision digital processing, and a power-efficient embedded platform. At its core is a transimpedance amplifier (TIA) based on an electrometer-grade op-amp (ADA4530-1), enabling accurate conversion of ionization currents in the femtoampere range. A dual-path amplification architecture ensures dynamic range adaptability across low- and high-dose-rate conditions. The digital subsystem—featuring a 16-bit sigma-delta analog-to-digital converter (ADC)-equipped STM32 microcontroller—handles real-time digitization, temperature compensation, and self-adjustment offset via integrated digital-to-analog converters (DACs). The device was calibrated and tested at the Secondary Standard Dosimetry Laboratory (SSDL) of Turkish Nuclear Energy Research Institute (TENMAK), covering a wide radiation range from 3 μSv/h to 60 mSv/h using multiple ^{137}Cs sources. The system demonstrated excellent linearity ($R^2 > 0.998$), with a minimum detectable dose rate of approximately 2 μSv/h, and maintained a total measurement error below 10%. These results affirm the device's suitability for portable, high-precision radiation monitoring in field and safety applications. The novelty of this work lies in the integration of a high-pressure argon IC with a dual-path femtoampere readout front-end and a fully self-adjusting digital control unit, enabling portable, low-dose-rate detection below 3 μSv/h.**

***Index Terms*—Analog circuits, digital circuits, ionization chamber (IC), low-level current measurements, microcontrollers, radiation measurements.**

I. Introduction

IONISATION chambers (ICs) are widely employed in fields where accurate measurement of ionizing radiation is essential, including medical physics, the nuclear industry, and environmental monitoring. Their ability to generate a current proportional to the absorbed dose rate renders them reliable for dose assessment and compliance with radiation safety regulations [1], [2], [3], [4], [5], [6], [7].

Received 7 August 2025; revised 1 December 2025; accepted 19 December 2025. Date of publication 26 January 2026; date of current version 23 February 2026. This work was supported by Turkish Energy Nuclear and Mineral Agency (TENMAK), Nuclear Energy Research Institute, under Grant A2.H1.P8. The Associate Editor coordinating the review process was Dr. Anna Case. *(Corresponding author: R. Bıyık.)*

R. Bıyık is with the Energy Institute, Department of Nuclear Research, Istanbul Technical University, 34475 Istanbul, Türkiye (e-mail: rbiyik@itu.edu.tr).

T. Yalçın is with the Department of Software Engineering, Istanbul Sabahattin Zaim University, 34303 Istanbul, Türkiye (e-mail: tamer.yalcin@izu.edu.tr).

O. Alaçayır is with Turkish Energy Nuclear and Mineral Agency (TENMAK), Nuclear Energy Research Institute, 34303 Istanbul, Türkiye (e-mail: osman.alacayir@tenmak.gov.tr).

Digital Object Identifier 10.1109/TIM.2026.3657559

One of the primary challenges in IC-based radiation meters—particularly for low-dose-rate applications—is achieving sufficient sensitivity to detect extremely low ionization currents in the femtoampere to picoampere range [8], [9]. To overcome this, high-pressure chambers filled with inert gases are typically used to enhance signal strength [10]. However, converting these weak signals into meaningful dose measurements requires a precision analog front-end, a stable high-voltage supply, and an effective signal readout architecture [11], [12], [13].

Traditional IC systems often rely on bulky analog electronics, external power supplies, and limited portability, restricting their usability in field operations [14]. Although microcontroller-based dosimetry systems have improved accessibility and integration, they frequently compromise measurement precision or analog signal quality.

Building upon the first phase of our project—where a high-pressure IC was designed and characterized in terms of linearity, saturation, recombination, and gas pressure dependence—this study presents the second phase, focusing on the development of a compact, battery-powered, high-precision IC-based radiation meter [15].

The proposed system uses a high-precision transimpedance amplifier (TIA) to convert ultralow ionization currents into measurable voltage while minimizing noise. The analog signal chain, featuring programmable gain and offset trimming, optimizes the dynamic range. Unlike conventional instruments relying on bulky electrometers, the proposed design combines high-pressure ionization physics with a dual-path analog front-end and digital baseline correction—representing a novel approach to simultaneously achieving high sensitivity and portability.

The system is designed for field usability thanks to its compact form factor, robust power management, and energy-efficient operation. The unit is powered by a rechargeable lithium-ion battery, supported by integrated charging and voltage regulation for stability. The low-power e-paper display enhances readability under various lighting conditions. These features make it a highly integrated, portable dosimetry solution ideal for applications such as occupational protection, emergency response, and environmental surveillance.

II. System Overview

The proposed electronic readout system comprises three main components as follows.

1) A high-pressure cylindrical IC (filled with 10 bar argon gas).
2) An analog front-end board for current signal acquisition and conditioning.

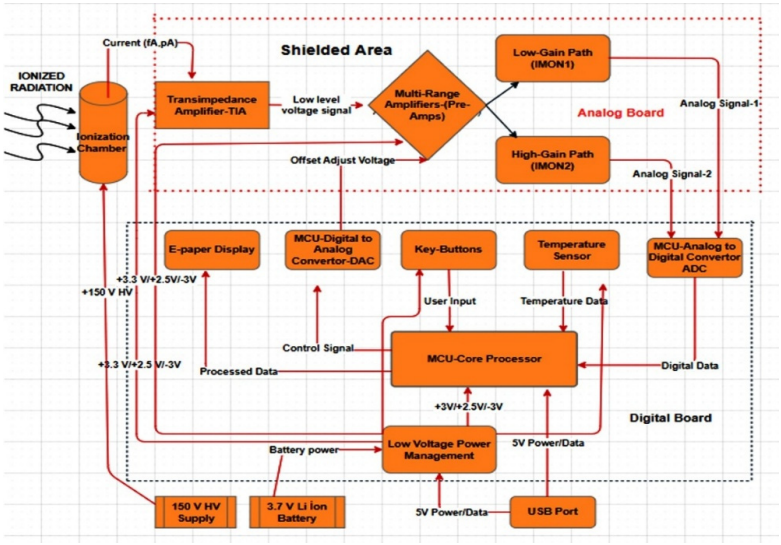

Fig. 1. Functional block diagram of the portable high-pressure ion chamber radiation detection system. The system comprises a pressurized ion chamber (filled with argon), a TIA, dual-gain analog signal paths (IMON1 and IMON2), and a digital control and processing section.

3) A digital control board responsible for data sampling, USB communication, power management, and display control.

The working principle of the system (Fig. 1) can be summarized as follows.

Radiation present in the environment interacts with the argon gas inside the IC, generating a minute ionization current proportional to the dose rate. This current is converted into a voltage signal by a TIA on the analog board. The signal is then fed into two parallel amplification paths (IMON1 and IMON2), each with different gain factors, to support a wide dynamic measurement range.

The resulting analog voltages are digitized by the high-resolution sigma-delta analog-to-digital converters (ADCs) integrated into the microcontroller unit (MCU) on the digital board. The MCU processes this data, applies digital filtering algorithms, and performs temperature compensation using real-time data from an onboard temperature sensor. The final radiation dose rate is calculated and displayed on an energy-efficient e-paper display.

To ensure long-term accuracy, the system features a feedback-based self-adjustment offset mechanism. During the offset calibration mode, the MCU determines the system offset and sends correction voltages to the analog board via its internal digital-to-analog converters (DACs).

The entire system is powered by a dedicated power management module, which supplies regulated voltages from either a rechargeable 3.7-V lithium-ion battery or an external USB connection. The power unit ensures stable and low-noise supply rails required by both analog and digital subsystems.

III. Radiation Measurement System Components

A. Detector (Ionization Tube)

The IC employs a cylindrical aluminum housing with an effective collection volume of 320 cm^3 (Fig. 2). Its inner surface is electropolished to minimize charge trapping. A copper rod serves as the anode, while the chamber wall acts as the cathode. High-pressure argon gas is introduced via a pneumatic valve mounted on the chamber's lateral surface. The technical details of the ionization tube are provided in [15]. Upon exposure to ionizing radiation, the pressurized argon gas generates electron–ion pairs. A 150-V bias applied between the anode and cathode ensures efficient charge collection. The resulting current is converted to voltage by the TIA and digitized downstream.

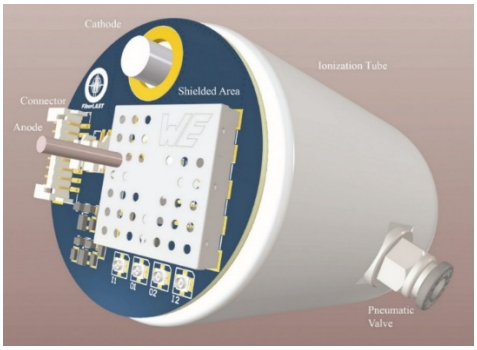

Fig. 2. 3-D rendered view of the integrated IC and analog front-end electronics, showing the high-pressure argon-filled tube, anode–cathode terminals, connector interface, signal-conditioning circuit, shielded section, and pneumatic gas valve.

B. Analog Board

The analog front-end circuitry, shown in Fig. 3, is designed to convert the extremely low-level current signals in (fA–pA range) produced by the IC into measurable voltages suitable for digitization via an ADC. The analog board consists of four primary functional blocks. The most critical among them is the TIA stage.

1) Transimpedance Amplifier: The TIA is the first stage in the signal chain and is responsible for converting the input current from the IC into a voltage [Fig. 3(a)]. For the TIA configuration, the ARZ electrometer-grade operational amplifier (U3) was selected due to its ultralow input bias

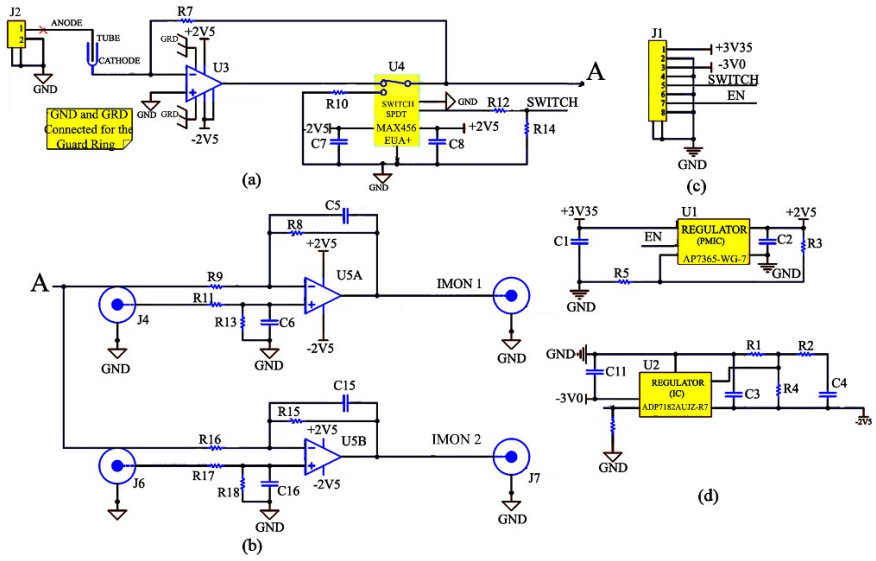

Fig. 3. Analog front-end schematics. (a) TIA (U3 ADA4530-1) and switch (U4 MAX4364) for measurement/calibration control. (b) Dual-gain amplifiers (U5A/B LTC2055HV) with OFFSET1/2 adjustment. (c) Connector J1 links power and control lines to the digital board. (d) Regulators U1 (+ 2.5 V) and U2 (–2.5 V) for op-amp supply.

current (on the order of 10^{-15} A), making it well suited for high-impedance, low-current measurement applications [12], [16], [17].

The current-to-voltage conversion is governed by the transimpedance gain, defined by the feedback resistor R_f, as shown in the following relation:

$$V_o = -I_i \times R_f. \tag{1}$$

In this design, the feedback/shunt resistor $R_f(R_7)$ is the Ohmite SM102032007FE precision resistor (2 GΩ, ±1%, 25 ppm/°C) [Fig. 3(a)].

2) Analog Switch: The analog switch (MAX4364EUA+) is controlled by the MCU via the SWITCH signal [Fig. 3(a)]. During normal operation, it allows the TIA output to reach the preamplifier stages for real-time measurements. In calibration mode, the MCU toggles the switch to disconnect the TIA output and ground the preamplifier input. The residual output voltage—arising from component offsets—is measured and stored as the system offset. Subsequent readings are digitally corrected by subtracting this offset.

The device exhibits a low ON-resistance (< 40 Ω) and minimal charge injection (~5 pC), limiting switching artifacts. To suppress transients, the MCU discards the first few samples after switching. Resistor R_{10} (0 Ω) provides a defined path to ground during calibration, preventing floating nodes and ensuring stable baseline conditions. Overcurrent damage is inherently avoided since the ion chamber produces only fA–pA currents, and the ADA4530-1 includes input protection structures.

This switching mechanism is critical for maintaining the accuracy and stability of the system over time and under varying environmental conditions. It allows seamless transitions between measurement and calibration modes under firmware control, facilitating real-time offset correction and long-term drift compensation.

3) Multirange Amplification and Offset Adjustment: Following the TIA, the signal passes through two parallel amplification paths—U5A (low gain) and U5B (high gain)—implemented with LTC2055HV zero-drift amplifiers. Their ultralow offset and temperature drift characteristics make them ideal for near-DC radiation signals.

The MCU continuously monitors both output channels (IMON1 and IMON2) to support autoranging. During calibration, residual DC offsets are compensated by fine-tuned voltages applied via the MCU's integrated DACs to the OFFSET1 and OFFSET2 inputs.

This dual-path configuration extends the measurable dynamic range while preserving high resolution for ultralow currents, ensuring stable and repeatable performance across all radiation dose rates.

Offset Correction via DAC Control: To suppress residual DC offsets, the analog circuitry includes dedicated OFFSET1 and OFFSET2 input pins. During the instrument's calibration phase (i.e., in the absence of radiation-induced current), a DAC on the digital board applies fine-tuned correction voltages to these inputs.

The MCU initiates this process at start-up. It collects background signal data over a predefined sampling period, averages the measured voltages, and stores them as baseline offset values. These voltages are then actively subtracted from subsequent measurements through a summing amplifier configuration, thereby eliminating the influence of static offsets.

This automated offset compensation mechanism is vital for maintaining system accuracy—especially in high-impedance environments where femtoampere-level currents are being measured and where even minimal DC errors could result in substantial relative deviations.

4) Power Supply Circuit: High-precision analog signal acquisition requires clean, stable supply rails to minimize noise and drift in the measurement chain. As shown in Fig. 3(d), the analog board includes dedicated voltage regulation circuits to meet these stringent requirements. A low-noise negative voltage regulator (U1: ADP7182AUJ-R7) and a positive voltage regulator (U2: AP7365-WG-7) are employed to provide

regulated supply voltages for the TIA (U3), analog switch (U4), and amplification stages (U5A and U5B). Input voltages of + 3.35 and −3.0 V are delivered from the digital board via connector J1 [Fig. 3(c)]. After appropriate decoupling and filtering, these regulators generate clean ±2.5 V.

5) Noise Analysis of the Input Stage: The most critical limitation in femtoampere-level current detection is the noise performance of the TIA. The ADA4530-1, chosen for its ultralow bias current (~20 fA) and low noise, minimizes this effect. The main TIA noise sources are expressed as [18] and [19].

Johnson (Thermal) Noise of the Feedback Resistor:

The feedback resistor $R_f = 2\ G\Omega$ introduces a thermal noise voltage given by [19]

$$e_{n,R} = \sqrt{4kTR_f\Delta_f} \tag{2}$$

where $k = 1.38 \times 10^{-23}\ J/K, T = 300$ K, and Δ_f is the measurement bandwidth. For $R_f = 2 \times 10^9\ \Omega$ and $\Delta_f = 1$ Hz

$$e_{n,R} \approx .58\ \mu V_{\text{rms}}/\sqrt{\text{Hz}}.$$

This corresponds to an equivalent input current noise of

$$i_{n,R} = \frac{e_{n,R}}{R_f} \approx .29\frac{\text{fA}}{\sqrt{\text{Hz}}}.$$

The op-amp input current and voltage noise densities are approximately 0.1 and 0.01 fA/(Hz)$^{1/2}$, respectively, which is negligible compared to the resistor's Johnson noise.

Considering the dominant resistor noise, the overall noise current density is approximately

$$i_{n,\text{total}} \approx 3\ \text{fA}\Big/\sqrt{\text{Hz}}\ .$$

The effective measurement bandwidth was determined by the digital moving average filter implemented in firmware, which corresponds to an equivalent noise bandwidth of approximately 10 Hz under standard sampling conditions (averaging window of 100 ms). For a measurement bandwidth of 10 Hz (after digital filtering), the expected rms input noise current is

$$i_{n,\text{RMS}} \approx 9.5\ \text{fA}.$$

This corresponds to an output noise voltage of

$$V_{n,\text{out}} = i_{n,\text{RMS}} \times R_f \approx .19\ \mu V.$$

Experimental results from the Secondary Standard Dosimetry Laboratory (SSDL) calibration (Section IV) indicate that a radiation dose rate of 1 μSv/h corresponds to a current of approximately 15–20 fA. Since the calculated rms input noise is below this level, the system is capable of detecting dose rates above 2–3 μSv/h without being noise-limited.

Furthermore, guarding techniques, PCB shielding (Faraday cage), and digital filtering implemented in the MCU reduce low-frequency leakage and external EMI/RFI interference, ensuring that practical noise levels remain consistent with the theoretical estimation. Experimental baseline measurements conducted under zero-radiation conditions confirmed this estimation. The observed rms output fluctuation of approximately 45–55 μV at the TIA output closely matched the predicted Johnson noise level calculated for a 2-GΩ feedback resistor and 10-Hz bandwidth.

In addition, repeated baseline measurements ($n = 10$) were performed under identical environmental conditions to statistically assess system noise. The resulting rms voltage fluctuation of 45–55 μV at the TIA output corresponds to a standard deviation of 22 μV ($k = 1$), consistent with the theoretical Johnson noise level for a 2-GΩ feedback resistor within a 10-Hz bandwidth.

6) PCB Layout and Shielding Considerations: In femtoampere-level current measurement circuits, PCB layout and material choices are as critical as the active components themselves. The design presented here incorporates several noise-mitigation and leakage-suppression strategies.

Guarding: The input node and feedback network of the TIA are surrounded by a continuous copper guard ring actively driven to the same potential as the op-amp input, preventing leakage currents across the PCB surface [20], [21].

Faraday Cage Shielding: The TIA stage and the ultrahigh-value feedback resistor are enclosed within a perforated metal Faraday cage mounted at the center of the analog PCB. This enclosure protects the circuit from external electric fields, EMI/RFI coupling, and static charges, which would otherwise overwhelm fA-level signals.

Analog-to-Digital Separation: The analog and digital ground planes are isolated and connected at a single star point to minimize ground-loop noise. Signal routing between the ion chamber, analog front-end, and digital board is kept as short as possible to reduce parasitic capacitance and inductive pickup.

Direct Mounting: The analog PCB is mounted directly above the IC to minimize the physical distance between the chamber electrodes and the TIA input. This arrangement reduces parasitic leakage paths and helps maintain signal integrity.

Material Selection: The PCB substrate and solder mask were selected for low leakage properties, and critical input traces were designed with wide clearance to further suppress surface currents.

Collectively, these measures ensure that the realized noise performance closely matches the theoretical noise floor of the TIA, thereby enabling stable and accurate measurement of ionization currents at the femtoampere scale.

C. Digital Board

The digital board acts as both the processing unit and the power management hub of the device (Fig. 4). Its architecture consists of functionally isolated blocks designed to manage data acquisition, control signals, communication, and calibration logic.

1) MCU—STM32F373CCT6 (U1A/U1B): The digital core relies on the STM32F373CCT6 mixed-signal processor (ARM Cortex-M4), chosen specifically for its on-chip integration of precision analog and digital control, which ensures high-fidelity measurements [22]. Key features include integrated 16-/12-bit ADCs for high-resolution digitization and dual DACs for fine calibration and offset adjustments.

Supported by robust communication interfaces and efficient DMA, this low-power MCU handles all system aspects—from signal processing and calibration routines to user interaction and data transmission—within a single, deterministic framework [23], [24].

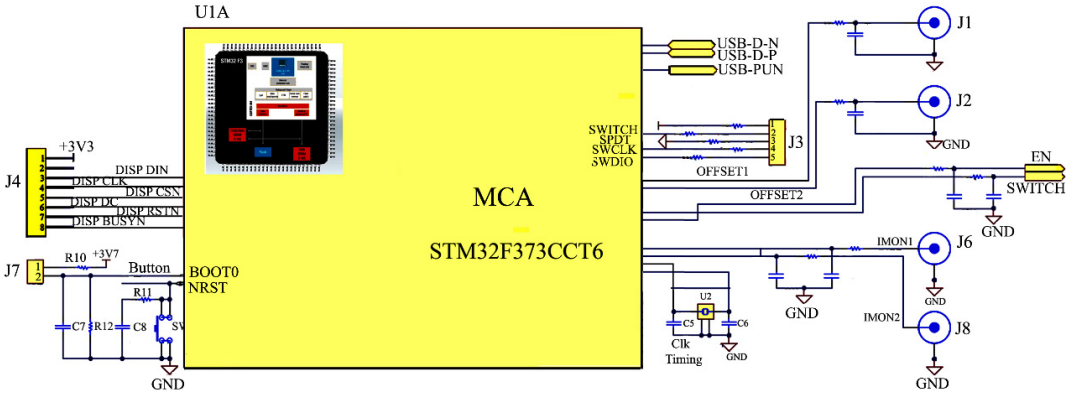

Fig. 4. Digital board schematic integrating STM32F373CCT6 MCU with peripheral circuits, including BOOT/reset, analog board interfaces (OFFSET1/2, SWITCH, and IMON1/2), USB and I^{2}C communication, display driver, power lines, and ADC-/DAC-based calibration and control.

2) Measurement and Digitization: A core function of the MCU is the precise digitization of analog signals (IMON1 and IMON2) via integrated 16-bit sigma-delta ADCs (SDADCs), which are vital for high accuracy. The 16-bit resolution (65 536 levels) provides a 16-fold resolution improvement over typical 12-bit ADCs, enabling the detection of extremely low radiation currents. Crucially, the sigma-delta architecture suppresses noise through oversampling and digital filtering, ensuring a cleaner, more stable, and reliable digital representation of the input signal.

3) Calibration and Control: The MCU also executes closed-loop system calibration using its dual 12-bit DACs. During calibration, the MCU switches the preamplifier input to a grounded reference (zeroing mode) via a GPIO pin to calculate the offset error. The DACs then generate and apply precise correction voltages to actively compensate for measured bias offsets, thereby ensuring continuous self-correction against drift caused by aging, temperature variation, or supply instability.

4) Computation and Logic: The ARM Cortex-M4 core manages dynamic range by continuously sampling both low-gain (IMON1) and high-gain (IMON2) channels simultaneously at ten samples per second. The firmware employs automatic gain switching with 10% hysteresis (switching from high to low gains at >85% full-scale and back at <75%) to prevent oscillation and maintain data continuity. During these rapid transitions (which take less than 100 ms), a five-sample moving average digital smoothing function is applied to ensure a seamless and stable displayed dose rate across the entire dynamic range. Furthermore, the MCU uses additional digital filtering (moving average and median filters) to suppress noise and improve measurement repeatability.

The system also supports temperature compensation by reading an external I^{2}C sensor and applying a predefined linear correction factor. This factor primarily corrects for the temperature coefficient of key analog components (feedback resistor and op-amp drift). Although the current prototype uses a simple correction, the firmware architecture is designed to accommodate future comprehensive multiparameter temperature characterization to enhance long-term stability.

5) Interface and Communication: The MCU manages user interaction and system communication using several peripherals: GPIO lines handle button input and e-paper display control; the I^{2}C bus reads the temperature sensor; and the USB controller provides host communication, firmware upgrade (bootloader mode), and battery charging functionality. These interfaces ensure robust autonomous operation and external maintainability.

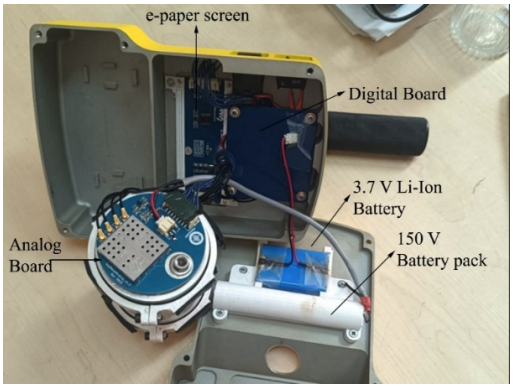

Fig. 5. Internal structure of the portable IC detector showing integrated analog and digital boards, e-paper display, 3.7-V lithium-ion system battery, and 150-V bias pack. The modular design ensures compactness and portability without loss of sensitivity.

D. Power Architecture: Multistage and Low-Noise Power Tree

The multistage power architecture efficiently manages energy for both analog and digital subsystems. All supply voltages are derived from two main sources: a 3.7-V lithium-ion battery for low-voltage circuits and a 150-V bias voltage (derived from six series 25-V batteries) required for the IC (Fig. 5).

1) Battery Management and Protection: The 3.7-V lithium-ion cell is managed by dedicated ICs. The LTC4054 (U3) handles linear charging via the USB port, while the MAX6775 (U4) supervisor monitors voltage and uses MOSFET (Q1) to automatically disconnect the battery, preventing overdischarge and ensuring cell health [Fig. 6(a)].

2) Voltage Regulation Chain: The unregulated + 3.7-V output is processed by a hierarchical voltage regulation strategy to ensure clean, noise-free supply rails for the precision analog front-end. Key rails include the two-stage-regulated–3.0-V

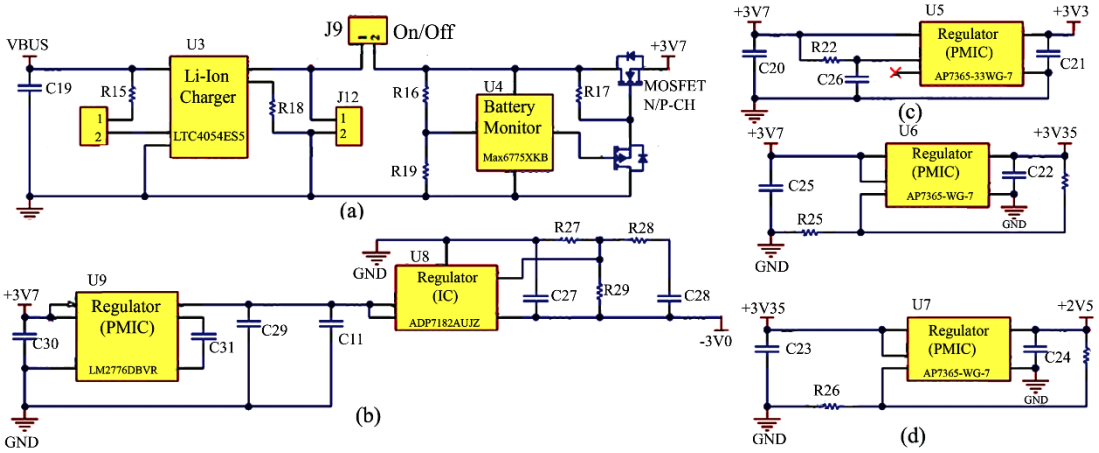

Fig. 6. Power management and regulation circuits. (a) Lithium-ion charging/protection via LTC4054 and MAX6775. (b) −3.0-V generation using LM2776 and ADP7182. (c) + 3.3-V digital regulator (AP7365). (d) Sequential LDOs providing + 3.35 and + 2.5 V for analog sections.

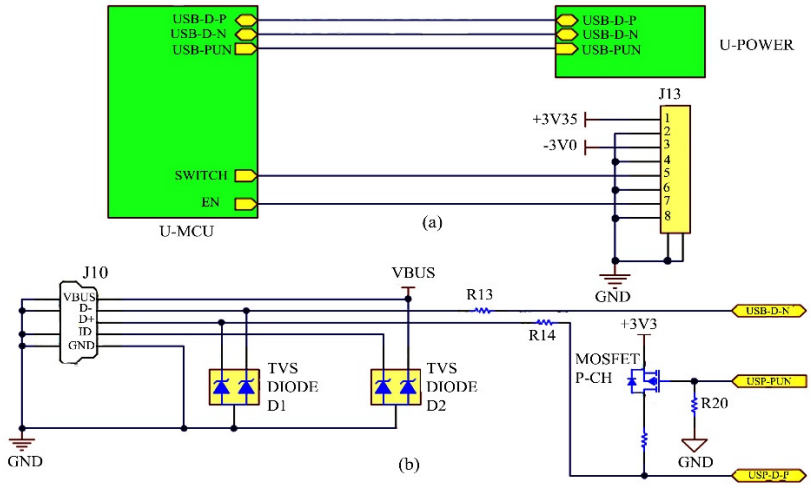

Fig. 7. USB connection and control circuitry. (a) Interface between the MCU and power module showing data, power, and enable lines. (b) USB socket with RCLAMP0502BATCT ESD diodes, series resistors, and pull-up network ensuring safe, stable communication.

analog supply (generated by an inverter U9 and LDO U8) for op-amps [Fig. 6(b)], the + 3.3-V digital supply (fixed LDO U5) for logic, and precision + 3.35- and + 2.5-V analog supplies (cascaded LDOs U6/U7) for sensitive analog components and the MCU's internal ADC/DAC (VDDA) [Fig. 6(c)]. This topology provides the low noise and high PSRR critical for femtoampere-level signal processing.

3) Analog-to-Digital Board Interfacing: Power and control signals are transmitted between the digital and analog boards via connectors J13 (digital) [Fig. 7(a)] and J1 (analog) [Fig. 3(c)]. This tightly integrated interface carries the critical + 3.35- and −3.0-V analog supplies, common ground, and essential MCU control signals: the SWITCH line (Pin 5) for calibration mode toggling and the EN line (Pin 7) for activating specific analog subsystems. This synchronization facilitates enhanced system responsiveness and measurement integrity.

E. USB Interface and Firmware Update Mechanism

The USB interface facilitates secure data communication and enables firmware upgrades via the MCU's native bootloader (activated by the BOOT0 button). The USB connector (J10) is designed for robust operation and safety, incorporating ESD protection diodes (D1 and D2) and a switching transistor (Q2) [Fig. 7(a) and (b)]. These direct connections and easy bootloader access provide a reliable, user friendly method for deploying software updates without external programming tools, ensuring long-term maintainability and field serviceability.

IV. System Testing and Calibration

The electronic readout system developed for the ion chamber detector tube was tested at the SSDL, part of the Nuclear Energy Research Institute under TENMAK. As an accredited institution and a member of the IAEA/WHO SSDL network, as well as the designated authority for ionizing radiation metrology within EURAMET, the SSDL provides the required infrastructure and traceability for high-accuracy dosimetry tests [25]. The measurements were conducted using calibrated ^{137}Cs sources with three different activity levels: 5.93 Ci (high), 2.49 Ci (medium), and 23.79 mCi (low). These allowed testing over a wide dose-rate range from 3 μSv/h to 60 mSv/h [26].

To evaluate the system response across the full dynamic range, the dose-rate intervals were classified as follows.

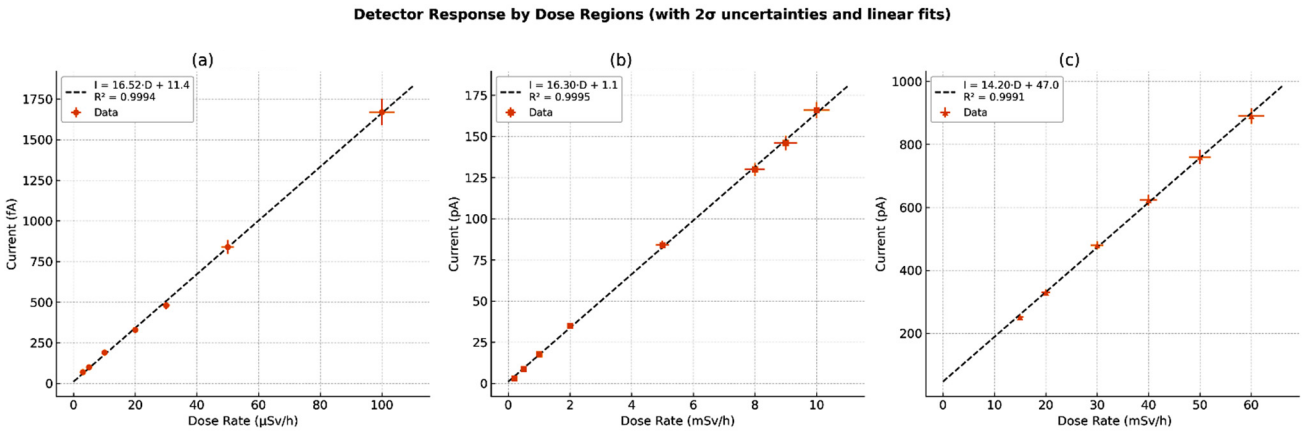

Fig. 8. Detector response as a function of dose rate in three regions. (a) Low (3–100 μSv/h), (b) medium (0.1–10 mSv/h), and (c) high (15–60 mSv/h). Each plot includes a linear regression fit with the corresponding equation (dotted line) and coefficient of determination (R^2). Error bars represent $\pm 2\sigma$ measurement uncertainties.

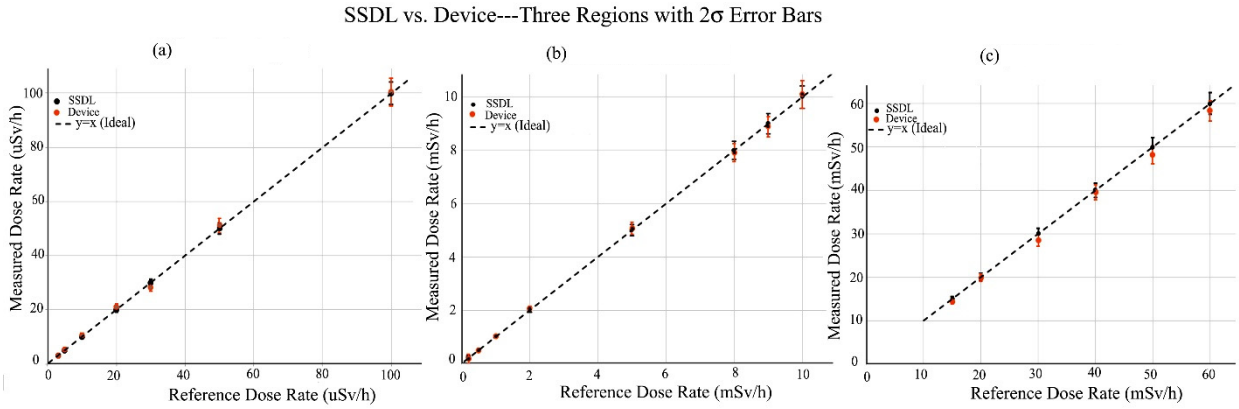

Fig. 9. Comparison of measured dose-rate values obtained from the developed IC system and the SSDL reference values across three regions. (a) Low dose (3–100 μSv/h), (b) medium dose (0.2–10 mSv/h), and (c) high dose (15–60 mSv/h). Error bars represent expanded uncertainties ($k = 2$). Orange markers represent the device measurements (with $\pm 2\sigma$ error bars), while black markers correspond to the SSDL reference values. The dashed line denotes the ideal response (y = x). The results demonstrate excellent linearity ($R^2 > 0.998$) and deviations below $\pm 10\%$ over the full dynamic range.

Low-Dose Rates: 3–100 μSv/h.
Medium-Dose Rates: 0.1–10 mSv/h.
High-Dose Rates: 20–60 mSv/h.

The corresponding current outputs from the detector were recorded and summarized in Table I. The results exhibit excellent linearity across the full dose-rate range, as demonstrated in Fig. 8.

A. ^{137}Cs Source Arrangement and Dose-Rate Generation

The radiation field used for calibration was generated using three sealed ^{137}Cs sources. Each source is housed within a dedicated, shielded containment unit integrated into a computer-controlled calibration system at the SSDL facility. Depending on the desired dose rate, the appropriate source is automatically moved from its shielded position to the irradiation position through a motorized mechanism. At the irradiation position, the gamma beam is collimated and directed toward the detector under test. The detector holder is also positioned automatically according to precalibrated exposure geometries that correspond to specific dose-rate points previously characterized using primary-standard reference dosimeters. For example, the 3-μSv/h exposure point corresponds to a predefined geometry–source configuration stored in the control system, ensuring precise and repeatable irradiation conditions. The expanded measurement uncertainty of the SSDL system, as reported by its accredited quality documentation, is 4.2% ($k = 2$) for low-dose-rate fields and 4.1% ($k = 2$) for medium- and high-dose-rate fields.

B. Obtaining the Device's Dose-Current Characteristics

Before irradiation, the detector's baseline (background) current was recorded under ambient conditions to determine offset levels. This baseline, including electronic and environmental noise, varied between 0.3 and 2 pA in repeated background measurements. Subsequently, the detector was exposed to the SSDL's calibrated ^{137}Cs fields at varying dose rates, and the corresponding ionization currents were recorded. For each dose rate, multiple on–off irradiation sequences were performed to verify repeatability. The background current was subtracted from raw readings to obtain net ionization current values, as listed in Table I. Before each new dose-rate exposure, the offset stability of the detector was monitored under identical environmental conditions. The offset current variation remained within 10–30 fA, confirming good short-term stability. Measurement uncertainty was calculated

TABLE I
MEASURED IONIZATION CURRENT VALUES AT DIFFERENT DOSE RATES OBTAINED FROM THE DEVELOPED SYSTEM DURING SSDL CALIBRATION TESTS

Low Dose Rate		Medium-Dose Rate		High Dose Rate	
Dose Rate±%4.2 ($k = 2$)(μSv/h)	Current (fA)	Dose Rate ±%4.1 ($k = 2$)(mSv/h)	Current (pA)	Dose Rate ±%4.1 ($k = 2$)(mSv/h))	Current (pA)
3±0.12	70±15	0.2±0.008	3.13±0.12	15±0.63	252±7.56
5±0.20	100±14	0.5±0.02	8.91±0.35	20±0.84	330±9.9
10±0.41	190±13	1±0.04	17.69±0.53	30±1.26	480±13.4
20±0.82	330±17	2±0.08	35±1.05	40±1.68	623±17.4
30±1.23	480±24	5±0.21	84±2.52	50±2.10	760±22.0
50±2.05	840±42	8±0.33	130±3.9	60±2.52	890±25.7
100±4.10	1670±82	9±0.37	146±4.38		
		10±0.42	166±4.98		

TABLE II
COMPARISON OF RADIATION DOSE-RATE MEASUREMENTS OBTAINED FROM THE DEVELOPED PORTABLE IC SYSTEM AND THE ACCREDITED SSDL REFERENCE DOSIMETER. REPORTED DIFFERENCES REPRESENT PERCENTAGE DEVIATIONS, INCLUDING MEASUREMENT UNCERTAINTIES ($k = 2$)

Low Dose Rate			Medium-Dose Rate			High Dose Rate		
[1]Dose Rate (μSv/h)	[2]Dose Rate (μSv/h)	[3]Diff. (%)	[1]Dose Rate (mSv/h)	[2]Dose Rate (mSv/h)	[3]Diff. (%)	[1]Dose Rate (mSv/h)	[2]Dose Rate (mSv/h)	[3]Diff. (%)
3±0.12	3.1±0.64	3.3	0.2±0.08	0.19±0.17	-5.2	15±0.63	14.43±0.65	-3.8
5±0.20	5.3±0.77	6.0	0.5±0.02	0.48±0.02	-4.1	20±0.84	19.92±0.82	-0.4
10±0.41	10.6±0.75	6.0	1±0.042	1.01±0.04	1.0	30±1.26	28.49±1.43	-5.3
20±0.82	21.1±1.06	5.5	2±0.084	2.07±0.07	3.4	40±1.68	39.56±1.74	-1.1
30±1.23	28.36±1.5	-5.4	5±0.21	5.08±0.22	1.5	50±2.10	48.21±2.12	-3.6
50±2.05	51.15±2.57	2.3	8±0.336	7.91±0.34	-1.1	60±2.52	58.36±2.32	-2.7
100±4.10	100.4±5.05	0.4	9±0.378	8.90±0.38	-1.1			
			10±0.42	10.11±0.52	1.1			

[1]SSDL:Secondary Standard Dosimetry Laboratory (reference system)
[2]Device:Developed Portable Ion Chamber System
[3] Deviation(%) $= \frac{\text{Device}-\text{SSDL}}{\text{Devise}} \times 100\%$

as the standard error of repeated readings, and all results are reported with their expanded uncertainties ($k = 2$).

As shown in Fig. 8, the results demonstrate excellent linearity across the entire dose-rate range. Error bars represent $\pm 2\sigma$ ($k = 2$) uncertainties obtained from repeated measurements under identical exposure conditions.

The data indicate that approximately 15–20 fA of ionization current was generated per 1 μSv·h^{-1}, which matches the 20-fA sensitivity threshold of the TIA used in the analog front-end. Hence, the system can reliably detect dose rates above 2–3 μSv·h^{-1}.

To convert the measured current (after background subtraction) into radiation dose rate, three linear calibration functions were derived for each of the three regions

$$\text{Low Dose} \quad I = 16.52 \times D + 11.4 \tag{3}$$

$$\text{Medium Dose} \quad I = 16.30 \times D + 1.1 \tag{4}$$

$$\text{High Dose} \quad I = 14.2 \times D + 47 \tag{5}$$

where I is the net ion current after subtraction of offset/background current fA for low-dose region, and pA for medium- and high-dose regions. D is the dose rate in μSv/h for low-dose region, and mSv/h for medium- and high-dose regions.

During operation, the system automatically performs background measurement at start-up or upon user request via the function button. The 30-s averaging period and digital filtering are applied to determine offset current, which is then subtracted from subsequent readings.

C. Calibration Results and Comparison With SSDL Reference

The developed system's dose-rate readings show excellent overall agreement with SSDL reference values across low, medium, and high ranges, confirming its wide dynamic response (Table II). The total measurement error remained below 10% at all test points, meeting the acceptance criteria for portable ion chamber dosimetry (Fig. 9) [27], [28].

Medium-Dose Region (0.1–10 mSv/h): This range demonstrated optimal performance, with measured points nearly overlapping the ideal 1:1 reference line, exhibiting the most stable linearity and minimal error.

Low-Dose Region (3–100 μSv/h): The response is highly linear and repeatable above 5 μSv/h. A slight overresponse below 20 μSv/h is noted, attributed to operating near the detection threshold, where noise and background subtraction increase relative uncertainty.

High-Dose Region (15–60 mSv/h): The system maintains the reference trend with minimal deviation, though a slight underresponse beyond 30 mSv/h suggests initial ion recombination/saturation effects. Despite this, the total deviation remains within the 10% tolerance.

D. Dose/Charge Relationship Factor ($F_{Q/D}$) Analysis

The dose/charge relationship factor ($F_{Q/D}$) is the fundamental calibration coefficient, quantifying collected electrical

charge per unit dose (C/μSv), and its stability confirms reliable dosimetric performance [29].

Average Values: The average $F_{Q/D}$ is approximately 6.6×10^{-11} μSv in the low-dose region (3–100 μSv/h) and 5.9×10^{-11} C/μSv in the medium-/high-dose region (0.2–60 mSv/h).

Optimal Linearity: The detector exhibits its most stable and linear behavior between 20 μSv/h and 20 mSv/h, with $F_{Q/D}$ clustering around 6.0×10^{-11} C/μSv.

Nonlinearity at Extremes: Below 20 μSv/h, $F_{Q/D}$ exhibits noticeable variability (peaking 8.4×10^{-11} C/μSv) attributed to noise and background current subtraction near the detection threshold. Beyond 30 mSv/h, the factor begins to decline, reaching a minimum of 5.34×10^{-11} μSv/h, which is consistent with ion recombination (saturation) effects. This quantified deviation provides the necessary data for applying high-dose correction factors.

V. Conclusion

A fully integrated, battery-powered ionization chamber readout system has been developed and validated for field use in radiation monitoring. The design achieves femtoampere-level current sensitivity, wide dynamic range, and excellent linearity across multiple radiation intensities.The system integrates: a precision transimpedance amplifier (TIA), dual-gain analog paths, and a mixed-signal microcontroller with high-resolution ADC and DAC modules.Together, these components enable the conversion of ultra-low ionization currents into stable and accurate dose-rate measurements.

An automated offset-correction and calibration algorithm ensures real-time accuracy and long-term stability.With additional features such as: USB-based firmware update, temperature-aware digital correction, ultra-low-power e-paper display, and compact, rechargeable form factor,the developed system offers a robust, portable, and high-precision solution for on-site radiation monitoring in health physics, nuclear safety, and environmental surveillance applications.

References

[1] G. F. Knoll, *Radiation Detection and Measurement*, 4th ed., Hoboken, NJ, USA: Wiley, 2010.

[2] X. Lang et al., "Characterization of real-time dose measurement using monitor ionization chamber in electron beam FLASH radiotherapy," *Nucl. Eng. Technol.*, vol. 57, no. 6, Jun. 2025, Art. no. 103551, doi: 10.1016/j.net.2025.103551.

[3] J. A. C. Gonçalves et al., "Activity measurements of 192Ir solid sources using a well-type ionization chamber," *Nucl. Instrum. Methods Phys. Res. A, Accel. Spectrom. Detect. Assoc. Equip.*, vol. 580, no. 1, pp. 222–225, Sep. 2007, doi: 10.1016/j.nima.2007.05.089.

[4] H. S. Kim, S. H. Park, J. H. Ha, Y. K. Kim, J. K. Kim, and S. Y. Cho, "Performance of a high-pressure xenon ionization chamber for environmental radiation monitoring," *Radiat. Meas.*, vol. 43, nos. 2–6, pp. 659–663, Feb. 2008, doi: 10.1016/j.radmeas.2007.12.040.

[5] X.-L. Dong, Z.-J. Ma, Z.-W. Jiang, Q. Wang, and R. Gou, "Small ion pulse ionization chamber for radon measurement in underground space," *Appl. Radiat. Isot.*, vol. 212, Oct. 2024, Art. no. 111467, doi: 10.1016/j.apradiso.2024.111467.

[6] L. P. Neves, A. P. Perini, and L. V. E. Caldas, "Development and characterization of a new cylindrical ionization chamber for dosimetry of ^{60}Co beams," *IEEE Trans. Nucl. Sci.*, vol. 60, no. 2, pp. 712–715, Apr. 2013, doi: 10.1109/TNS.2012.2219319.

[7] J. Radtke et al., "Ionization chambers to determine neutron and gamma-ray kerma in a research reactor," *IEEE Trans. Nucl. Sci.*, vol. 66, no. 10, pp. 2160–2169, Oct. 2019, doi: 10.1109/TNS.2019.2937750.

[8] N. Golnik, Z. Rusinowski, and M. Zielczynski, "Ionization chamber and measuring system for low-level dosimetry," in *Proc. 22nd Annu. Int. Conf. IEEE Eng. Med. Biol. Soc.*, vol. 4, Jul. 2000, pp. 3249–3252.

[9] T. Kawaguchi et al., "Low-level radiation measurement system with magnetically levitated electrode ionization chamber detector," *IEEE Trans. Nucl. Sci.*, vol. 53, no. 4, pp. 2276–2280, Aug. 2006, doi: 10.1109/TNS.2006.878572.

[10] P. Degtiarenko and V. Popov, "New techniques of low level environmental radiation monitoring at JLab," *IEEE Trans. Nucl. Sci.*, vol. 57, no. 5, pp. 2719–2723, Oct. 2010, doi: 10.1109/TNS.2010.2065238.

[11] C. P. M. Lim and E. D. Dimaunahan, "Implementation of a 32-channel low-cost low current measuring circuit using analog devices ADA4530-1 on automated test equipment for parallel leakage current test on semiconductor switch test platform conversion," in *Proc. IEEE Region 10 Symp. (TENSYMP)*, Aug. 2021, pp. 1–4, doi: 10.1109/TENSYMP52854.2021.9550815.

[12] L. Wei et al., "Picoampere level current detection for ultraviolet photoelectron spectroscopy instrument," in *Proc. Int. Conf. Sens., Meas. Data Anal. Era Artif. Intell. (ICSMD)*, Oct. 2024, pp. 1–4, doi: 10.1109/icsmd64214.2024.10920560.

[13] D. Drung and C. Krause, "Ultrastable low-noise current amplifiers with extended range and improved accuracy," in *Proc. Conf. Precis. Electromagn. Meas. (CPEM)*, Jul. 2016, pp. 1–2.

[14] S. K. Singh and M. S. Kulkarni, "Development of an ionization chamber for low and medium energy photon dosimetry," *Radiat. Protection Dosimetry*, vol. 182, no. 2, pp. 215–220, Dec. 2018, doi: 10.1093/rpd/ncy051.

[15] R. Bıyık, O. Alaçayır, T. Yalçın, and T. Tuna, "Development of a handheld pressurized ionization chamber for gamma monitoring," *Radiat. Meas.*, vol. 181, Feb. 2025, Art. no. 107385, doi: 10.1016/j.radmeas.2025.107385.

[16] *Femtoampere Input Bias Current Electrometer Amplifier ADA4530-1*, Analog Devices, Wilmington, NC, USA, 2024.

[17] C. Ryan and D. Foor, "Noise evaluation of various high-gain, very-low-noise current sense amplifier circuits," in *Proc. IEEE Aerosp. Conf.*, Mar. 2021, pp. 1–6, doi: 10.1109/AERO50100.2021.9438275.

[18] M. Štubian, J. Bobek, M. Setvin, U. Diebold, and M. Schmid, "Fast low-noise transimpedance amplifier for scanning tunneling microscopy and beyond," *Rev. Sci. Instrum.*, vol. 91, no. 7, pp. 1–11, Jul. 2020, doi: 10.1063/5.0011097.

[19] D. Walter, A. Bülau, and A. Zimmermann, "Review on excess noise measurements of resistors," *Sensors*, vol. 23, no. 3, p. 1107, Jan. 2023, doi: 10.3390/s23031107.

[20] *Low Level Measurements Handbook*, Keithley, Cleveland, OH, USA, 2004. [Online]. Available: https://www.keithley.com

[21] K. Meierbachtol et al., "Development of an ionization chamber for the SPIDER fission fragment detector," *Nucl. Data Sheets*, vol. 119, pp. 389–391, May 2014, doi: 10.1016/j.nds.2014.08.108.

[22] STMicroelectronics. (2015). *STM32F373xx, Datasheet-Production Data*. [Online]. Available: https://www.st.com

[23] Z. Wei, "Research on STM32-based signal conditioning system measurement system," *Highlights Sci., Eng. Technol.*, vol. 42, pp. 9–17, Apr. 2023.

[24] B. Zhang, Y. Jiang, Y. Li, X. Chen, and X. Wen, "Design and development of high precision magnetic encoder based on TMR MEMS device," in *Proc. IEEE 16th Int. Conf. Nano/Micro Eng. Mol. Syst. (NEMS)*, Apr. 2021, pp. 474–479, doi: 10.1109/NEMS51815.2021.9451506.

[25] *The IAEA/WHO Network of Secondary Standard Dosimetry Laboratories, SSDL Network Charter*, IAEA, Vienna, Austria, 1999.

[26] T. Zengin, D. Yaşar, E. Kapdan, S. Aydın, M. Korkmaz, and H. Erez, "The traceability for the reference standard dosemeter systems," *Engineer Machinery*, vol. 55, no. 653, pp. 43–59, 2014.

[27] Ludlum. *Ambient Dose Ion Chamber*. Accessed: 2025. [Online]. Available: https://ludlums.com/products/health-physics/product/model-9dpstar

[28] J. Cardoso, J. A. M. Santos, L. Santos, J. G. Alves, and C. Oliveira, "Characterization of an active dosemeter according to IEC 61526:2010," *Radiat. Protection Dosimetry*, vol. 170, nos. 1–4, pp. 127–131, Sep. 2016, doi: 10.1093/rpd/ncw090.

[29] R. Kranzer et al., "Charge collection efficiency, underlying recombination mechanisms, and the role of electrode distance of vented ionization chambers under ultra-high dose-per-pulse conditions," *Phys. Medica*, vol. 104, pp. 10–17, Dec. 2022, doi: 10.1016/j.ejmp.2022.10.021.